https://doi.org/10.1016/j.ymssp.2022.109571

# Bi-objective optimal design of an electromagnetic shunt damper for energy harvesting and vibration control

Ruqi Sun, Waion Wong*, Li Cheng
Department of Mechanical Engineering
The Hong Kong Polytechnic University, Hong Kong, PRC

## Abstract:

Owing to the electromechanical energy conversion capacity, electromagnetic shunt dampers (EMSDs) are widely applied to vibration suppression or energy harvesting from vibrating structures. Either one of the two functions can be optimized in the designs of EMSD found in the literature. In this paper, a bi-objective optimization methodology of EMSD is proposed for the simultaneous maximization of energy harvesting from the damper and the suppression of resonant vibration of a dynamic structure. An EMSD with opposing magnet pairs configuration is designed to achieve the two design objectives simultaneously in a single-degree-of-freedom (SDOF) system and a dynamic vibration absorber (DVA). It is proved analytically and experimentally that maximum energy can be harvested by the EMSD when its internal impedance equals to the external electrical resistance of the electrical circuit. Minimum resonant vibration amplitude of the primary mass can be achieved at the same resistance ratio in the DVA system by selecting the suitable number of opposing magnet pairs of the EMSD without affecting the internal resistance. An EMSD with opposing magnet pairs configuration is designed and tested in a single-degree-of-freedom (SDOF) system and a dynamic vibration absorber. Following a proper procedure, the electromechanical transduction factor of the proposed EMSD can be tuned to achieve both objectives simultaneously. The harvested energy is higher when the EMSD is deployed in the SDOF system than in the DVA system, but the frequency bandwidth for energy harvesting is much wider in the DVA system. Analyses lead to a design guideline of the EMSD for achieving the bi-objective optimization.

## Keywords:

Bi-objective optimal design, Energy harvesting, Vibration control, Electromagnetic shunt damper, Dynamic vibration absorber

---

* Corresponding author.
E-mail address: mmwowong@polyu.edu.hk (Waion Wong)

**Nomenclature:**

| | | | |
|---|---|---|---|
| $B$ | Magnetic flux density | $B_r$ | Radial magnetic flux density |
| $B_z$ | Vertical magnetic flux density | $c_1$ | Damping coefficient of primary system |
| $c_2$ | Damping coefficient of DVA system | $C_{dr}$ | Coefficient between damping and resistance |
| $c_e$ | Damping coefficient of EMSD | $c_p$ | Parasitic damping coefficient |
| $d_1$ | Internal diameter of coils | $d_2$ | External diameter of coils |
| $d_{wire}$ | Wire diameter | $f$ | Excitation frequency in Hz |
| $F_0$ | Excitation force amplitude | $k_1$ | Stiffness of primary system |
| $k_2$ | Stiffness of DVA system | $K_t$ | Transduction factor |
| $L_{in}$ | Internal inductance of coils | $L_{wire}$ | Wire length |
| $m_1$ | Mass of primary system | $m_2$ | Mass of DVA system |
| $M_a$ | Number of opposing magnet pairs | $M_{ij}$ | Mutual inductance of two single coil *i* and *j* |
| $N$ | Turns of coils | $r_R$ | Resistance ratio |
| $R_{in}$ | Internal resistance of coils | $R_{load}$ | External resistance |
| $S$ | Cross-sectional area of wire | $x_1$ | Displacement of primary mass |
| $x_2$ | Displacement of DVA mass | $X$ | Displacement amplitude |
| $Z$ | Circuit impedance | $Z_{in}$ | Inductive impedance of EMSD coils |
| $\gamma$ | Natural frequency ratio ($\omega_{n2}/\omega_{n1}$) | $\gamma_{opti}$ | Optimal natural frequency ratio |
| $\delta_{ij}$ | Kronecker delta function | $\delta_{st}$ | Static deflection under constant force $F_0$ |
| $\varepsilon$ | Electromotive force | $\lambda$ | Frequency ratio between $\omega_n$ and $\omega_{n1}$ |
| $\mu$ | Mass ratio between $m_2$ and $m_1$ | $\xi$ | Damping ratio |
| $\xi_{opti}$ | Optimal damping ratio | $\rho$ | Electrical resistivity of copper |
| $\omega$ | Excitation frequency in rad/s | $\omega_{n1}$ | Natural frequency of primary system |
| $\omega_{n2}$ | Natural frequency of DVA system | | |

# 1. Introduction

As an energy dissipation device in vibrating systems, a damper is often used for vibration suppression by transferring vibration energy into other kinds of energy. Traditional viscous dampers provide damping force with the generation of heat. However, damping tunability is required in many applications due to the changes of working conditions. In a single-degree-of-freedom (SDOF) vibration system, the transmissibility varies differently with damping in different frequency ranges. Moreover, in a dynamic vibration absorber (DVA) system, only a specific amount of damping can keep the DVA working at the optimal condition [1]. High tunability of damping will benefit the onsite calibration of DVA system in real applications to prevent the detuning of the DVA due to changes of the working environment.

Traditional viscous dampers cannot work well in applications which require high damping tunability because its damping force is difficult to be varied. The emerging electromagnetic shunt damper (EMSD), which is firstly proposed by Behrens [2], can provide more flexibilities in adjusting its damping force by varying the electrical resistance in the damper circuit. With the flexible tunability of the damping coefficient that the proposed EMSD offers, the transmissibility of the primary SDOF system can be switched from maximum damping to minimum damping by switching the EMSD circuit from closed to open [3]. Eventually, a nonlinear EMSD can be designed for better isolation performance at non-resonant frequencies [4]. Moreover, the damping-sensitive DVA can also be implemented with the tunable EMSD [5]. All these point to some real applications, including civil frame structures [6], bridge cables [7], automobile suspension [8], aerospace engineering [9], etc. Different from a piezoelectric shunt damper with constant transduction factor, the transduction factor of EMSDs can be adjusted and tactically tuned by changing its volume. As a result, EMSD show great promise in coping with applications in large-scale dynamic structures.

The commonly used opposing magnets configuration of linear EMSD has been proved effective for transduction factor enhancement when compared with the homodromous magnets configuration [3]. The optimal opposing magnets pair is also investigated [10] to achieve the maximum transduction factor and damping coefficient. Based on the variable transduction factor with different opposing magnets pairs, the suitable configuration is selected to achieve the bi-objective optimization for energy harvesting and vibration control in this paper. More explorations for enhancing the transduction factor include adding magnetic guiding materials [11] to increase the magnetic flux through the coils, using Halbach magnet array [12] to concentrate the magnetic field on target position, etc.

An EMSD can also be utilized as an energy harvester with the capacity of transferring kinetic energy to electrical energy. The vibration energy from dynamic systems like vehicle suspensions [13,14], railway tracks [15] and human motions [16,17] can be harvested through EMSD devices. The dual functions of a tunable damper and energy harvester allow EMSD to be used for vibration control and energy harvesting simultaneously [18-21]. For energy harvesting, it is noticed that the maximum harvested energy occurs when the external impedance equals to the internal impedance of the EMSD circuit [22], while the vibration amplitude usually remains large. An EMSD is tuned to provide the highest damping force when it is designed for vibration suppression, in which case, however, the external resistance is zero and no energy can be harvested. Therefore, existing EMSDs usually work at optimum conditions to accommodate one design objective in the open literature. Theoretically, if the EMSD parameters are properly adjusted, it is possible to obtain the optimal amount of damping and get maximum harvested energy in DVA systems. The minimization of structural kinetic energy and the maximization of the power dissipation in the DVA for slightly damped structures has been reported [23]. Some theoretical analyses and numerical simulations have been provided to discuss the power-based optimization for DVA with

EMSD [24]. An EMSD was applied to damp down bridge stay cable vibration and at the same time harvest some of the vibration energy but it cannot be optimized to achieve both objective simultaneously [25]. To the best of our knowledge, there is no real design and experimental proof of the bi-objective optimal EMSD reported in the open literatures. The proposed DVA with EMSD shows great promise as a promising device for both vibration mitigation and energy harvesting.

This is the motivation of the research work presented in this paper. A bi-objective optimal design methodology of EMSD is proposed and experimentally verified. Since the output power reaches the maximum value when the external resistance equals to the internal electrical resistance leading to the maximum energy harvesting by the EMSD. The proper number of EMSD opposing magnet pair is then selected to reach the optimal damping without affecting the coil internal resistance. A prototype of the proposed EMSD is built and tested in a SDOF vibrating system, and a 2-DOF vibrating system with a DVA mounted on a SDOF system. The optimum external resistance is found to be 6Ω at which bi-objective status of the EMSD is achieved in the DVA system. Meanwhile, the energy harvesting capacity in the DVA system can also be maintained at a relatively high level with a wider frequency range than SDOF system. Since the DVA system response is sensitive to the damping changes, the friction effects is minimized by using the nylon tube while fabricating the EMSD and aligning the concentricity of the EMSD components. Self-locking may occur at vibrations of low frequency and amplitude due to the friction effect [26,27], which should be avoided in the applications of the EMSD.

The two major contributions of this manuscript are follows. 1) This paper proposes a general design procedure of DVA system with EMSD to achieve the bi-objective optimization of simultaneous vibration suppression and energy harvesting. Previous studies [19-22] on DVA design only allows one objective to be optimized. Similarly in our previous work, an optimization method [10] of a DVA system with EMSD was also materialized for vibration suppression only. Therefore, simultaneously accommodating both functions through optimization based on EMSD is a novel contribution to the existing literature. 2) This paper proposes a method to derive the optimal number of magnet pairs of the EMSD to achieve the aforementioned bi-objectives. The key point here is to tune the transduction factor of the EMSD without affecting its coil resistance which is associated with the harvested power output.

In the following sections, a theoretical analysis on the energy harvesting of SDOF and DVA systems with EMSD is conducted, with a mission to provide necessary transduction factor adjustment of the EMSD without affecting the internal resistance of its coil. Subsequently, the suitable number of opposing magnet pairs is searched by numerical simulation and verified by experimental measurement. Finally, the proposed EMSD is applied to both SDOF and DVA system, and bi-objective optimal status in both test cases is reached and verified through experiments.

## 2. Theoretical analyses

The theoretical basis underpinning an EMSD and the energy harvesting principles are briefly introduced in this section. The governing equations for vibration control when the EMSD is deployed in a SDOF and DVA system are derived. The principle of the proposed bi-objective optimal design is also described.

### 2.1 EMSD concepts and energy output

The basic model of EMSD with opposing magnets configuration [3] in Fig. 1(a) can be regarded as a linear damper. The main structure of the EMSD contains opposing magnets and the corresponding coil as illustrated in Fig. 1(a). The induced voltage $\varepsilon$, also called electromotive force (EMF), is generated by the relative velocity between the series-wound magnets and the coils, expressed as

$$\varepsilon = K_t \dot{x} \tag{1}$$

where $K_t$ denotes the transduction factor and $\dot{x}$ the relative velocity. When the coil is connected to a tunable resistor, the corresponding damping coefficient $c_e$ can be written as

$$c_e = \frac{K_t^2}{Z} = \frac{K_t^2}{R_{in} + R_{load}} \tag{2}$$

where $Z$ denotes the total impedance of the circuit. The inductance of the EMSD circuit as derived in section 3.2.1 is found to be very small in comparison with the internal resistance and therefore it is neglected in the calculation of the total impedance of the circuit. $R_{load}$ is the external resistance, and $R_{in}$ is the internal resistance of the EMSD circuit.

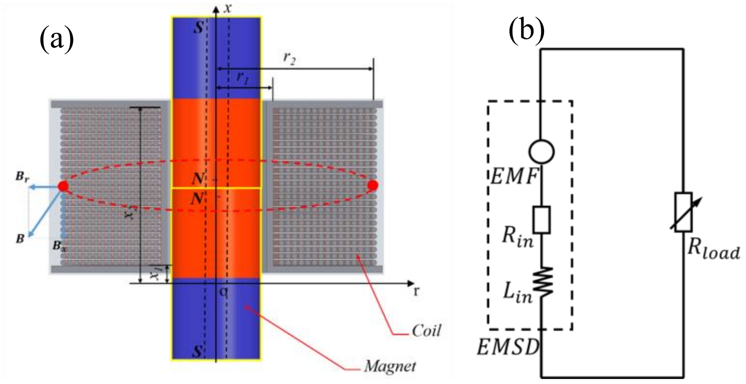

Fig. 1. EMSD with opposing magnet configuration: (a) main structures, (b) schematic diagram

Since the amount of energy dissipated by the internal resistance of the coil is fixed and difficult to be harvested, the output power of the harvested energy from the EMSD is only obtained from the dissipated energy of the external resistance. The root mean square of the output power can be expressed as

$$P_{rms} = \frac{\varepsilon^2 R_{load}}{2\left(R_{in} + R_{load}\right)^2} = \frac{\varepsilon^2}{2Z_{in}} \frac{r_R}{\left(1+r_R\right)^2} \tag{3}$$

The first and second derivative of $P_{rms}$ can be derived as

$$\frac{dP_{rms}}{dr_R} = \frac{\varepsilon^2}{2R_{in}} \cdot \frac{1-r_R^2}{\left(1+r_R\right)^4} \tag{4}$$

$$\frac{d}{dr_R}\left(\frac{dP_{rms}}{dr_R}\right) = \frac{\varepsilon^2}{R_{in}} \cdot \frac{r_R - 2}{\left(1+r_R\right)^4} \tag{5}$$

where $r_R = R_{load}/R_{in}$ is the resistance ratio between the external resistance and internal impedance. Let the first derivative equal to zero, we get $r_R = 1$. Then substituting $r_R = 1$ to the second derivative in Eq. (5), the value of second derivative becomes negative. Therefore, there is a maximum value of $P_{rms}$ at $r_R = 1$.

## 2.2 SDOF system with EMSD

When the EMSD is used as a tunable damper in the SDOF vibrating system as shown in Fig. 2. The equation of motion writes

$$m_1\ddot{x}_1 + c_1\dot{x}_1 + k_1x_1 = F_0\cos\omega t \tag{6}$$

where $m_1$, $k_1$, $c_1$ and $F_0$ denote the mass, stiffness, damping coefficient and excitation force amplitude of the system, respectively. Both the damping coefficient $c_e$ of the EMSD and the parasitic damping $c_p$ (including the friction damping and air damping) contribute to the total damping coefficient $c_1$ expressed as

$$c_1 = c_e + c_p \tag{7}$$

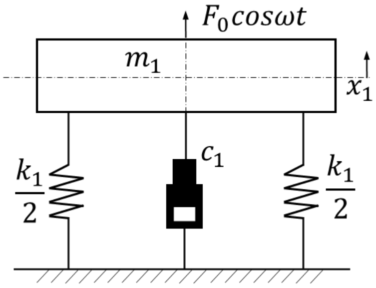

Fig. 2. Single-degree-of-freedom (SDOF) vibrating system

The displacement amplitude $X_1$ can be deduced by solving Eq.(6), yielding

$$X_1 = \frac{\delta_{st}}{\sqrt{\left(1-\lambda^2\right)^2 + \left(c_1\lambda/\sqrt{k_1 m_1}\right)^2}} \tag{8}$$

where $\delta_{st} = F_0/k_1$ denotes the static deflection of the spring under the static force $F_0$. $\lambda = \omega/\omega_{n1}$ is the excitation frequency ratio. The maximum amplitude $X_{max}$ of $m_1$ at resonance occurs when $\lambda = 1$. $X_{max}$ with different resistance ratio can be derived using Eqs. (2) and (8) as

$$X_{\max} = \left(F_0/\omega_n\right)\frac{1+r_R}{K_t^2/R_{in} + c_p\left(1+r_R\right)} \tag{9}$$

The first and second derivative of $X_{max}$ can be derived as

$$\frac{dX_{\max}}{dr_R} = \frac{\left(F_0K_t^2\right)/\left(\omega_n Z_{in}\right)}{\left[K_t^2/R_{in} + c_p\left(1+r_R\right)\right]^2} > 0 \tag{10}$$

$$\frac{d}{dr_R}\left(\frac{dX_{\max}}{dr_R}\right) = \frac{-2F_0K_t^2c_p\left[K_t^2/R_{in} + c_p\left(1+r_R\right)\right]}{\left(\omega_n R_{in}\right)} \le 0 \tag{11}$$

The $X_{max}{\sim}r_R$ relationship is a monotonically increasing parabolic function. Particularly, if $c_p = 0$, the second derivative equals to zero, the $X_{max}{\sim}r_R$ relationship becomes a linear function.

The normalized output power and the maximum displacement with the EMSD in the SDOF system are calculated using Eqs. (3) and (9) and plotted in Fig. 3. The plots show that the resonant vibration amplitude of the mass increases monotonically with the increase of resistance ratio, but the output power has a maximum value when the external resistance equals to the internal impedance of the EMSD, i.e. $r_R = 1$.

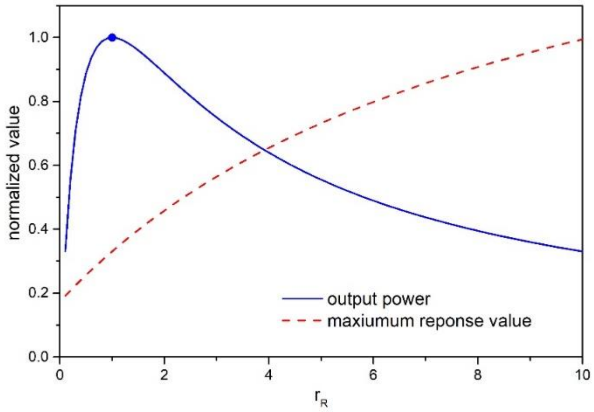

Fig. 3. Normalized output power and maximum displacement response with different resistance ratio

### 2.3 DVA system with EMSD

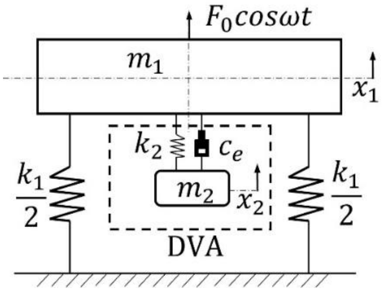

Fig. 4. Dynamic vibration absorber (DVA) system

Using EMSD as a tunable damper in the vibrating system in Fig. 4. The equations of motion may be written as

$$m_1\ddot{x}_1 + k_1 x_1 + k_2\left(x_1 - x_2\right) + c_e\left(\dot{x}_1 - \dot{x}_2\right) = F_0\cos\omega t \tag{12}$$

$$m_2\ddot{x}_2 + k_2\left(x_2 - x_1\right) + c_e\left(\dot{x}_2 - \dot{x}_1\right) = 0 \tag{13}$$

where $m_2$,$k_2$ and $c_e$ denote the mass, stiffness, and damping coefficient of the DVA, respectively. The amplitude ratio $|X_1/\delta_{st}|$ is written as [1]

$$G(\lambda,\xi) = \left|\frac{X_1}{\delta_{st}}\right| = \sqrt{\frac{\left(2\xi\lambda\right)^2 + \left(\lambda^2 - \gamma^2\right)^2}{\left(2\xi\lambda\right)^2\left[\left(1+\mu\right)\lambda^2 - 1\right]^2 + \left[\mu\gamma^2\lambda^2 - \left(\lambda^2 - 1\right)\left(\lambda^2 - \gamma^2\right)\right]^2}} \tag{14}$$

The corresponding optimal natural frequency ratio and damping ratio can be expressed respectively as

$$\begin{cases} \gamma_{opti} = \dfrac{1}{1+\mu} \\ \xi_{opti} = \sqrt{\dfrac{3\mu}{8\left(1+\mu\right)}} \end{cases} \tag{15}$$

The damping ratio of the DVA with the tunable EMSD can be derived by substituting Eq. (2) into the damping ratio $\xi$ written as

$$\xi = \frac{K_t^2}{2R_{in}\sqrt{k_2 m_2}\,(1+r_R)} = C_{dr}\frac{1}{(1+r_R)} \tag{16}$$

where $C_{dr} = K_t^2/\left(2Z_{in}\sqrt{k_2 m_2}\right)$ describing $\xi$ - $r_R$ relationship.

The bi-objective optimal status can be implemented by substituting $\xi_{opti}$ of Eq. (15) into (16) and setting $r_R = 1$. The corresponding optimal $C_{dr}$ can be expressed as

$$C_{dr\_opti} = \sqrt{3\mu/2(1+\mu)} \tag{17}$$

In practice, the optimal value $C_{dr\_opti}$ can be achieved by the fine tuning of other parameters of the EMSD as dictated by Eq.(16). Since the resistance ratio $r_R = 1$ is required for maximum energy harvest by the EMSD and $k_2$ and $m_2$ are not convenient to be adjusted, the transduction factor $K_t$ is the parameter used to tune the $C_{dr}$ to its optimal value $C_{dr\_opti}$ as shown in Eq. (17) above. The detail procedure of adjusting $K_t$ to achieve $C_{dr\_opti}$ is presented in section 3.

Albeit the optimal is obtained through Eq. (17), the variation of the primary system response with damping is still uncertain. Since the main concern is the relationship between $G(\lambda,\xi)$ and $\xi$, the effect of frequency can be eliminated by equaling the partial derivative with respect to frequency to zero.

$$\frac{\partial G(\lambda,\xi)}{\partial\lambda} = 0 \tag{18}$$

With the substituted $\mu$ and $\gamma_{opti}$ based on Eq. (15), the relationship between $\lambda$ and $\xi$ can be obtained by solving Eq. (18). In this case, all extreme values of $G(\lambda,\xi)$ with variable $r_R$ can be obtained by taking the $\lambda \sim \xi$ relational expression and Eq. (16) back to Eq. (14).

Assuming the mass ratio $\mu$ = 0.1, possible extreme values of $G(\lambda,\xi)$ with variable $\xi$ are calculated using Eqs. (14), (15) and (18) and plotted as the dash curves in Fig. 5. When the damping ratio $\xi < \xi_{opti}$, the solid response curves of $G(\lambda,\xi)$ versus $\lambda$ show two peaks with higher peak values at higher frequencies as shown by the red dash curve in Fig. 5. Therefore, the maximum values that locate at the red dash curve are the global maximum of the response amplitude of the primary mass. When $\xi > \xi_{opti}$, the solid response curves of $G(\lambda,\xi)$ versus $\lambda$ have only one peak. Denoted by the red dash line. To sum up, the red dash line is the global maximum response curve with the damping ratio $\xi$ varying from zero to infinity.

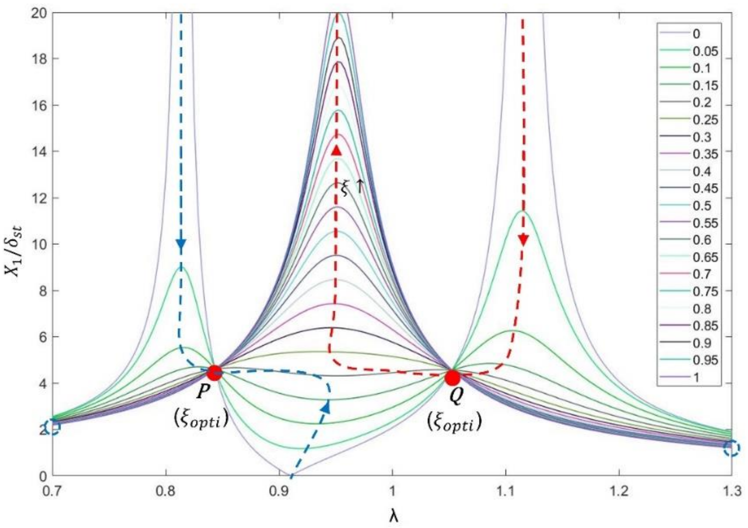

Fig. 5. Primary system response $G(\lambda,\xi)$ with different damping ratio in frequency domain (solid lines), and the stationary points connected lines (dash lines) based on the solved $\lambda \sim \xi$ relationship with Eq. (18), the vector denotes the increasing direction of damping ratio

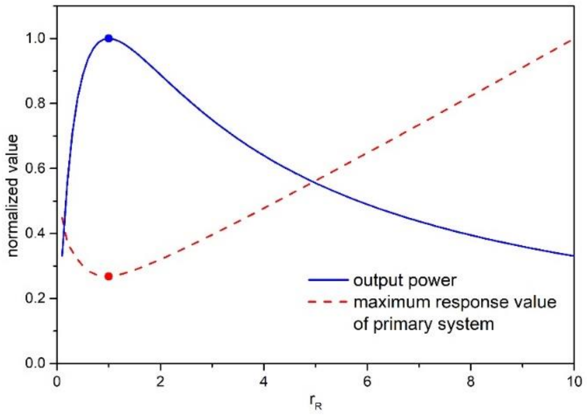

Fig. 6. Normalized value of the output power and the maximum amplitude of the primary system after adjustment of the constant $C_{dr}$

By substituting the damping ratio $\xi$ with the resistance ratio $r_R$ in Eq. (18), the relationship between $\max\{G(\lambda,\xi)\}$ and $r_R$ can be obtained as the red dash line in Fig. 6. The $C_{dr}$ of the EMSD in Eq. (16) can be tuned to the optimum value $C_{dr\_opti}$ according to Eq. (17) by properly adjusting the value of $K_t$. The output power of the EMSD as depicted by Eq. (3) is plotted as the blue curve in Fig. 6 as well. Since both the extreme values of the two curves in Fig. 6 locate at $r_R = 1$, the bi-objective of maximum output power from the EMSD and minimum resonant vibration of the primary system can be achieved simultaneously.

## 3. Design Analyses of EMSD Configurations

As mentioned above, the bi-objective optimal design of EMSD can be achieved by tuning $C_{dr}$ to its optimum value according to Eq (17). $C_{dr}$ can be adjusted by changing the value of transduction factor $K_t$ which depends on the design and the size of the EMSD. Due to the limitation of the space available for the EMSD in real applications, size variation of EMSD is most likely impractical. Therefore, an alternative design of the EMSD is used for the adjustment of $K_t$. As an example, the opposing magnets configuration in Fig. 1 provides a feasible way because $K_t$ can be varied by changing the number of opposing magnets in the EMSD without affecting its overall dimensions.

### 3.1 EMSD with opposing magnets pairs

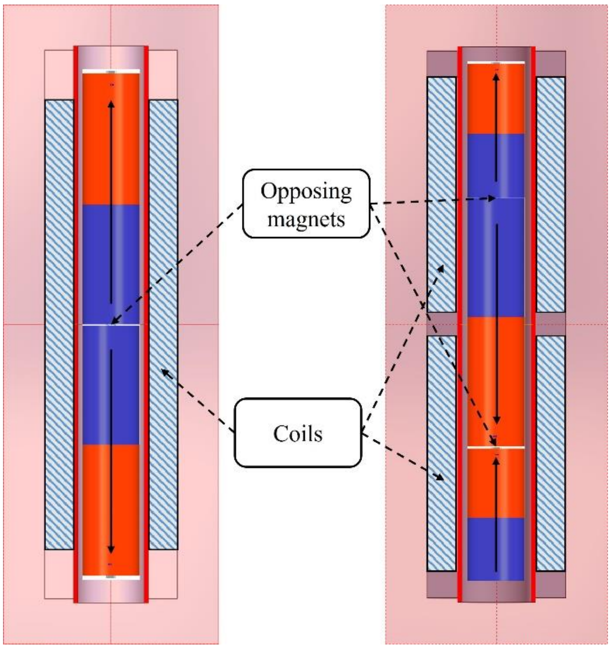

Fig. 7. EMSD schematics with one and two opposing magnet pairs configurations

As shown in Fig. 7, two EMSD designs of the same total length of magnets and coils have one and two opposing magnet pairs, respectively. Two independent coils around each magnet pair are connected with 180° phase difference. The polarization direction of each magnet pair is shown by a black solid arrow in the figures. To obtain the maximum transduction factor, the connection surface of the opposing magnet poles is located at the central points of each coil in the axial direction. The similar EMSD with six opposing magnet pairs is shown in Fig. 8. The pre-compressed DVA springs at the two ends of the magnet stack guide the motions of the magnets and the connected counter-weight to move along the axis of the EMSD. Moreover, a nylon tube is inserted between the magnets and coils as bearing in order to minimize the friction damping between the moving and stationary components of the EMSD.

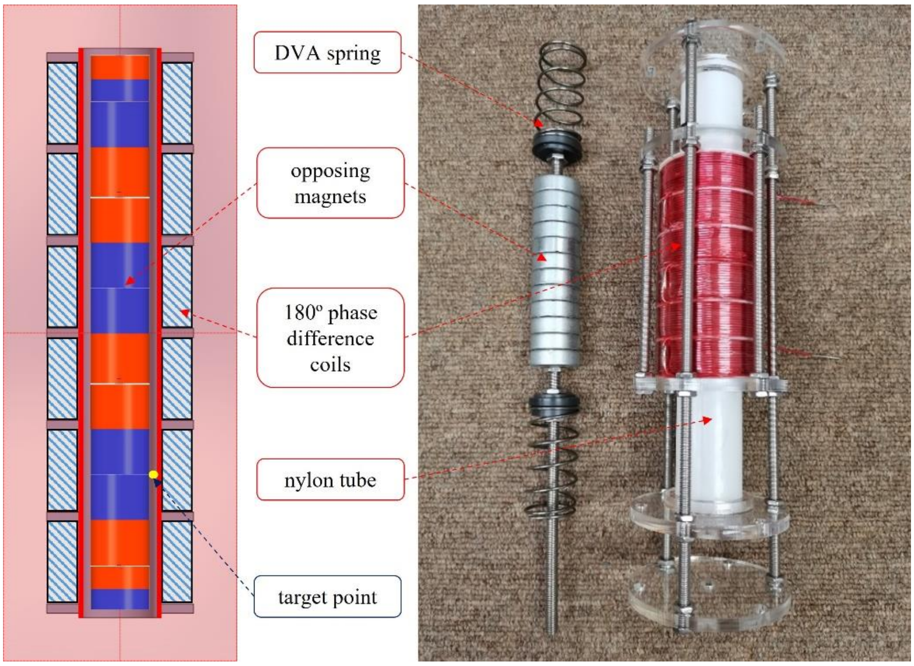

Fig. 8. EMSD with six opposing magnet pairs configuration: (a) schematic, (b) prototype

### 3.2 Parameter calibration of EMSD

The proposed EMSD is designed and tuned to work in the DVA in Section IV.A under the bi-objective optimal tuning condition for a SDOF vibration system. Since $C_{dr}$ is related to the DVA stiffness and mass, the parameters of the DVA system need to be identified before the structural parameter calibration of the EMSD.

The stiffness $k_1$ and $k_2$ of the primary system and the DVA are determined by linear fitting of the measured force-displacement data, while other parameters in Table 1 are calculated based on Eq. (15).

The calculated optimal damping coefficient for the DVA system is 8.8149 $\mathrm{N \cdot s/m}$. Therefore, the task is to design a tunable EMSD that can provide this damping when the external resistance equals to the internal impedance of the EMSD circuit. The total damping in the DVA includes the damping from the EMSD and the parasitic damping. Therefore, the damping coefficient of EMSD should be less than the required optimal damping coefficient.

Table 1. Identified parameters of DVA system

| | | |
|---|---|---|
| Measured parameters | $k_1$ | 20961 $\mathrm{N/m}$ |
| | $k_2$ | 1521.3 $\mathrm{N/m}$ |
| Calculated parameters | $m_1$ | 5.054 kg |
| | $m_2$ | 0.432 kg |
| | $\omega_{n1}$ | 64.4 $\mathrm{rad/s}$ |

| | | |
|---|---|---|
| | $\omega_{n2}$ | $59.3\ \mathrm{rad/s}$ |
| | $\mu$ | 0.0855 |
| | $\gamma_{opti}$ | 0.9212 |
| | $\xi_{opti}$ | 0.1719 |
| | $c_{opti}$ | $8.8149\ \mathrm{N \cdot s/m}$ |

Since the tunable range of the EMSD is significantly affected by the internal impedance of the coils based on Eq.(2), the impedance $Z_{in}$ should be minimized such that a higher damping coefficient can be provided by the EMSD. A common way to reduce the coil impedance is to use a thicker copper wire for the coil windings with sufficient turns to provide the EMF required in the EMSD circuit. A copper wire of 1mm diameter is used in the EMSD coil windings in the prototype, and the internal diameter of the coil is about 30 mm. A nylon tube is added to minimize the friction between the magnets and the coils. *NdFeB* N33 magnet with a coercivity ranging between 600 kA/m and 820 kA/m is used to construct the opposing magnet pair stack. The actual coercivity of the magnets can be determined from the measured superficial magnetic flux density. Other parameters of the EMSD are listed in Table 2. Six different opposing magnet pairs configurations (1, 2, 3, 4, 6 and 12 magnet pairs) are investigated for offering suitable $K_t$.

Table 2. The parameters of EMSD

| | | |
|---|---|---|
| Magnet parameters | Type & grade | *NdFeB* N33 |
| | Internal diameter | 6 mm |
| | External diameter | 24.5 mm |
| | Length | 8 mm |
| | Number | 12 |
| Nylon tube parameters | Internal diameter | 27 mm |
| | External diameter | 31 mm |
| Skeleton parameters | Internal diameter | 31 mm |
| | External diameter | 33 mm |
| | Height | 98 mm |
| Coil parameters | Internal diameter($d_1$) | 33 mm |
| | External diameter($d_2$) | 50 mm |
| | Total length($l_c$) | 90 mm |
| | Turns($N_{total}$) | 720 |
| | Wire diameter($d_{wire}$) | 1 mm |
| | Wire length($L_{wire}$) | 95 m |

### *3.2.1 Internal impedance of the coil*

The internal impedance of the coil mainly includes the internal resistance $R_{in}$ and the inductive impedance $2\pi f L_{in}$. It can be expressed as

$$R_{in} = \rho \frac{L_{wire}}{S} = \rho \frac{L_{wire}}{\pi \left( d_{wire}/2 \right)^2} \tag{19}$$

where $\rho = 0.0175\ \Omega \cdot \mathrm{mm}^2/\mathrm{m}$ is the electrical resistivity of copper.

Existing research on low-frequency vibration control with EMSD usually ignores the inductive impedance of the EMSD circuit because of its small value at low frequencies. However, the inductive impedance in the circuit cannot be neglected because the bi-objective optimal condition of the EMSD requires a certain resistance ratio of the circuit. Since the adjacent coils are connected with $180°$ phase difference, the total internal inductance should include the mutual inductance among the coils and the coil self-inductance [28], written as

$$L_{in} = \sum_{i=1}^{M_a} L_i \pm 2 \sum_{i=1}^{M_a} \sum_{j=1}^{M_a} M_{ij} \times \left( 1 - \delta_{ij} \right) \tag{20}$$

where $\delta_{ij} = 1$ for $i = j$, otherwise $\delta_{ij} = 0$; $M_a$ denotes the number of opposing magnet pairs, $L_i$ the self-inductance of the $i^{\text{th}}$ coil, $M_{ij}$ the mutual inductance between $i^{\text{th}}$ coil and $j^{\text{th}}$ coil. The plus or minus sign in Eq. (20) corresponds respectively to the phase difference $\Delta\phi$ of the coil at 0 or 180°. The mutual inductance of the coil is the multiple summations of the basic mutual inductance $M_{ij}$ of any two single coaxial coils $i$ and $j$.

The coil internal resistance and the internal inductance of different opposing magnet pair configuration can be calculated using Eqs. (19) and (20). The calculated results are shown in Table 3. The connection wire between the tunable resistors of the EMSD circuit is a bit long in this case with measured resistance about 0.3 Ω. It is considered as part of the internal resistance of the EMSD since no energy can be harvested from it.

Table 3. The coil impedance results comparison

| | Calculated results | Measured results |
|---|---|---|
| Internal resistance($R_{in}$) | 2.118 Ω | 2.087 Ω |
| Internal inductance($L_{in}$) | 2.18 mH | 1.274 mH |
| Resistance of connecting wire($R_{con}$) | 0.3 Ω | |
| Internal impedance($Z_{in}$) | 2.558 Ω | 2.469 Ω |

As shown in Table 3, the error between the calculated and the measured internal impedance is small. The average value of 2.5 $\Omega$ is selected as the nominal value for the calibration of other EMSD parameters. Moreover, since the heat generation of the electrical resistance of the coil can increases its internal impedance, the output power optimal status may locate at the point when the external resistance is slightly larger than the internal impedance of the coil at room temperature. After tuning for maximum energy harvesting, the optimal condition of vibration control can then be tuned to match with the energy harvesting optimal point by a proper adjustment procedure of the transduction factor $K_t$ described in the following section.

### *3.2.2 Transduction factor*

The transduction factor $K_t$ for the red single loop of the coil in Fig. 1 can be calculated according to its definition

$$K_t = -\oint_{loop} B_r\left(x,r\right)dl \tag{21}$$

where $B_r$ denotes the magnetic flux density. For the six opposing magnet pairs in Fig. 8, $K_t$ can be expressed as

$$K_t = -2\pi\sum_{j=1}^{M_a}\sum_{i=1}^{N} r\left(i,j\right)\left|B_r\left(x,r,i,j\right)\right| \tag{22}$$

where $M_a$ denotes the number of opposing magnet pairs and $N$ the number of turns for each coil.

As shown in Eq.(22), the calculation of $K_t$ requires the knowledge of the radial magnetic flux density distribution. The actual coercivity can be determined using the measured superficial magnetic flux density as mentioned above. The magnetic flux densities with different coercivities at the target point are shown in Fig. 8, together with the measured magnetic flux density obtained from a Gaussmeter in Fig. 9.

As shown in Fig. 9, the measured superficial magnetic flux density is 1.013 T, which equals the simulated value when the coercivity is around 780 kA/m. With the corrected coercivity, $K_t$ values obtained from different numbers of opposing magnet pairs are calculated according to Eq. (22) and shown as the blue dots in Fig. 10. The $K_t$ peaks at the two opposing magnet pairs configuration and decreases when the number of opposing magnet pairs is more than two. If any one of the configurations can provide the required optimal damping in Table 1 when the resistance ratio equals to one, then the bi-objective optimal design is achieved.

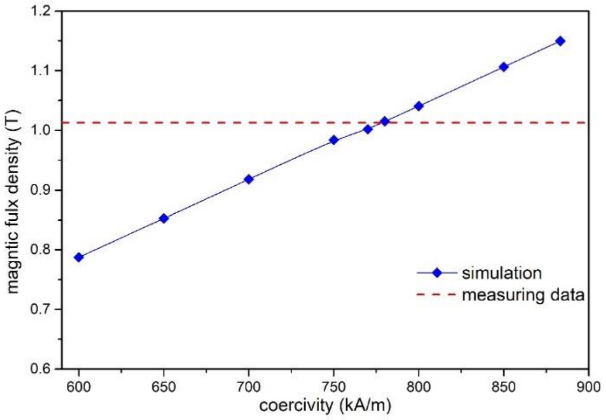

Fig. 9. Varied magnetic flux density with different coercivity and the measured superficial magnetic flux density

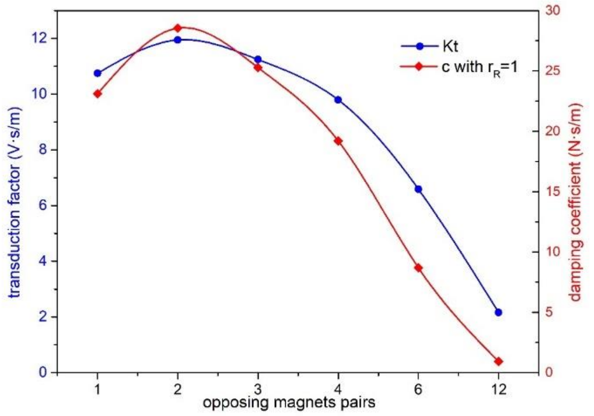

Fig. 10. EMSD transduction factor $K_t$ and damping coefficient $c_e$(when $r_R$=1) with different opposing magnet pairs

Moreover, the opposing magnets connecting surface is originally located at the central point of the coil along the axial direction as shown in Fig. 1. $K_t$ can be slightly tuned by changing the equilibrium position between the magnets and coils in the axial direction. As shown in Fig. 11, $K_t$ varies with different offset distances between the magnets and the coils. The original setting of locating the opposing magnets connecting surface at the central point of the coil can generate the largest $K_t$. While the offset distance increases in both positive and negative directions, $K_t$ decreases with a trend similar to a sine curve. The tunability of $K_t$ is conducive to the tuning of the optimal condition of the EMSD for vibration control of the primary system.

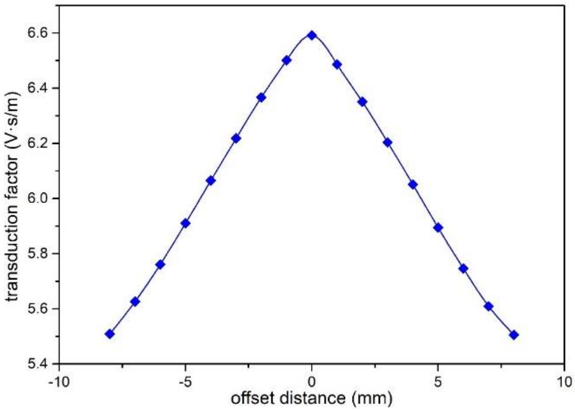

Fig. 11. Transduction factor $K_t$ at different offset distance between magnets and coils based on the original setting

### *3.2.3 Damping coefficient*

When $r_R = 1$ and $R_{load} = 2.5\,\Omega$, the damping coefficients with different numbers of opposing magnet pairs are calculated according to Eq. (2) and plotted as red rhombi connected curve in Fig. 10. The damping coefficient of the EMSD with six opposing magnet pairs configuration is found to be 8.7 $\mathrm{N \cdot s/m}$, which is nearest to the required optimal damping 8.8 $\mathrm{N \cdot s/m}$ in Table 1. Therefore, EMSD with six opposing magnet pairs in Fig. 8 is the most appropriate configuration to achieve the bi-objective optimal status. To verify the calculated results, this EMSD is tested with its damping coefficient measured.

The hysteresis loop of the proposed EMSD prototype is obtained by measuring the damping force and displacement of the EMSD with 10.25 Hz and 2 mm amplitude excitation and plotted in Fig. 12 to verify the accuracy of the simulated results. As shown in Fig. 12 (a) and (b), the friction in the EMSD varies significantly if the moving components are not carefully aligned to minimize the friction between the moving and non-moving parts of the EMSD. Fig. 12 (b) shows the hysteresis loop of minimum friction after careful alignment of the moving components such that the damping of the EMSD can be finely tuned by adjusting the transduction factor mentioned above to achieve the bi-objective optimal condition of the EMSD.

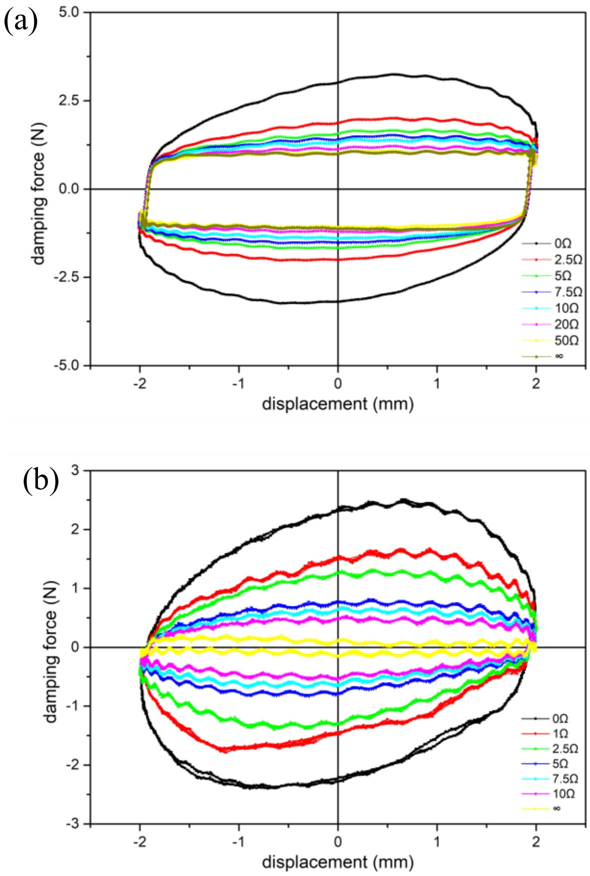

Fig. 12. Hysteresis loops of the proposed EMSD with (a) ordinary installation and (b) friction minimized installation

The value of the damping coefficient can be obtained from the energy lost per cycle in the EMSD as

$$c = \frac{\Delta U}{\pi \omega X} = \frac{U_1 - U_0}{2\pi^2 f X} \tag{23}$$

where $\Delta U$ is the energy loss, evaluated by the enclosed areas of the measured hysteresis loops in Fig. 12. $U_1$ denotes the energy lost with specific external resistance. $U_0$ denotes the energy loss when the circuit is open. $X$ is the displacement amplitude. $\omega$ and $f$ are the excitation frequencies in rad/s and Hz, respectively. In Fig. 12, displacement amplitude, $X = 2$ mm, excitation frequency, $f = 10.25$ Hz, and external resistance, $R_{load} = 2.5\ \Omega$. The energy loss $U_1$ - $U_0$ can be calculated using the enclosed areas of the hysteresis loops in Fig. 12. The damping coefficients of the EMSD can then be evaluated as $c_e = 8.69\ \mathrm{N \cdot s/m}$ and $8.81\ \mathrm{N \cdot s/m}$ for ordinary and friction minimized installations, respectively. The variation of the measured and simulated damping coefficients with different external resistances are shown in Fig. 13.

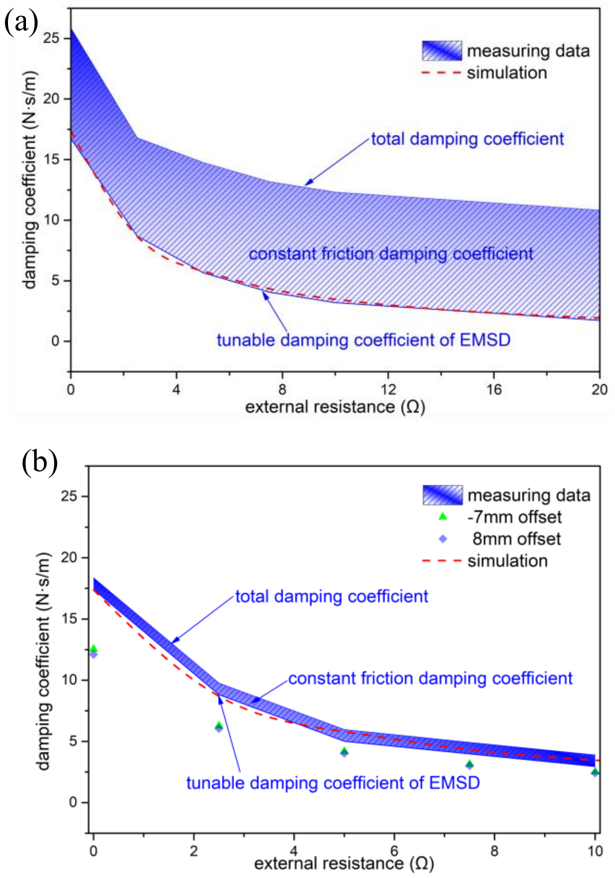

Fig. 13. Measured and simulated damping coefficient variation with different external resistance under different installations: (a) ordinary installation and (b) minimized friction installation

The friction effects can be minimized by carefully adjusting the installation angle and the location of the moving part in the damper as shown in Fig. 13. The transduction factor and the friction should be properly balanced to obtain the bi-objective optimal status. Moreover, the simulated results and the measured damping coefficient of the EMSD are matching well in both installations as shown in Fig. 13, which verified the modeling effectiveness of the proposed EMSD. The damping coefficient with offset distance is measured as shown in Fig. 13(b), when the EMSD is installed with minimum friction. The damping coefficients with -7 mm or 8 mm offset distances have smaller values than the ones without offset distance, which verified the offset displacement dependence of the damping coefficient predicted by the simulation results in Fig. 11.

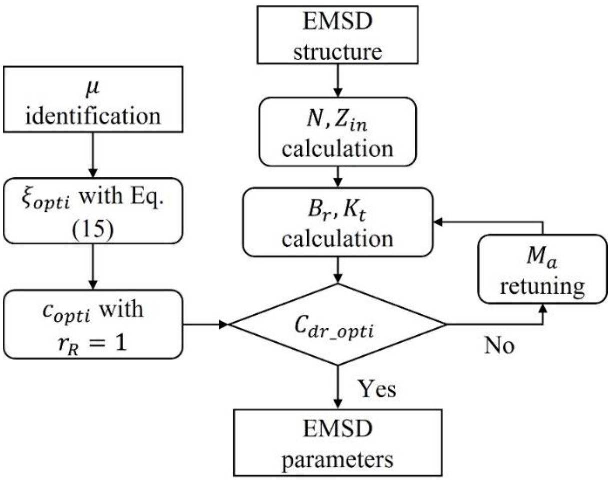

Fig. 14. Flowchart of the EMSD bi-objective optimal design procedure

With the theoretical and design analyses above, the bi-objective optimal design of EMSD requires two major steps (schematically represented in Fig. 14):

1. Determination of the constant $c_{opti}$.
2. Calibration of the EMSD parameters to satisfy $C_{dr\_opti}$.

## 4. Bi-objective experimental test of EMSD

The optimally designed EMSD is experimentally tested to verify the expected functionalities in terms of both vibration control in the SDOF system and energy harvesting in the DVA.

### 4.1 Experiment setup

The experimental setups of the SDOF system and DVA system are shown in Fig. 15. The non-contact exciter on the top provides the excitation force with negligible effect on the stiffness of the driven structure. A force sensor under the exciter is used for measuring the excitation force. Two laser sensors are fixed on a supporting holder to measure the displacement of the primary mass and the mass of the DVA. The pre-compressed DVA spring acts as a linear guide for the mass of the DVA. Four rotational bearings fix the primary system on the side faces and serve as a linear guide for the vibrating mass of the primary system with minimized friction. In the SDOF system, the coils of the EMSD are fixed on the mass plate of the primary system, while the magnets of the EMSD are fixed on the floor. In the DVA system, the coils of the EMSD are also fixed on the mass plate of the primary system, the magnets of the EMSD move inside the coils through the DVA spring. Moreover, both the magnets of the EMSD and the DVA counter-weight form the DVA vibrating mass. The effective values of both systems are tabulated in Table 1. The data acquisition system and the tunable resistor are shown in Fig. 16.

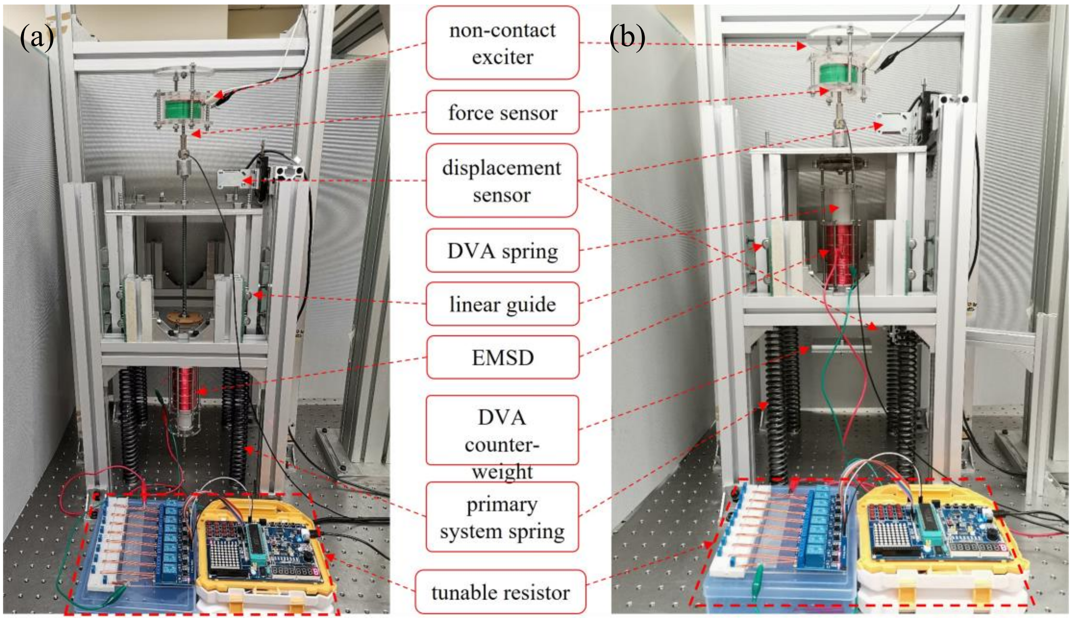

Fig. 15. Experimental setup: (a) SDOF system with EMSD, (b) DVA system with EMSD

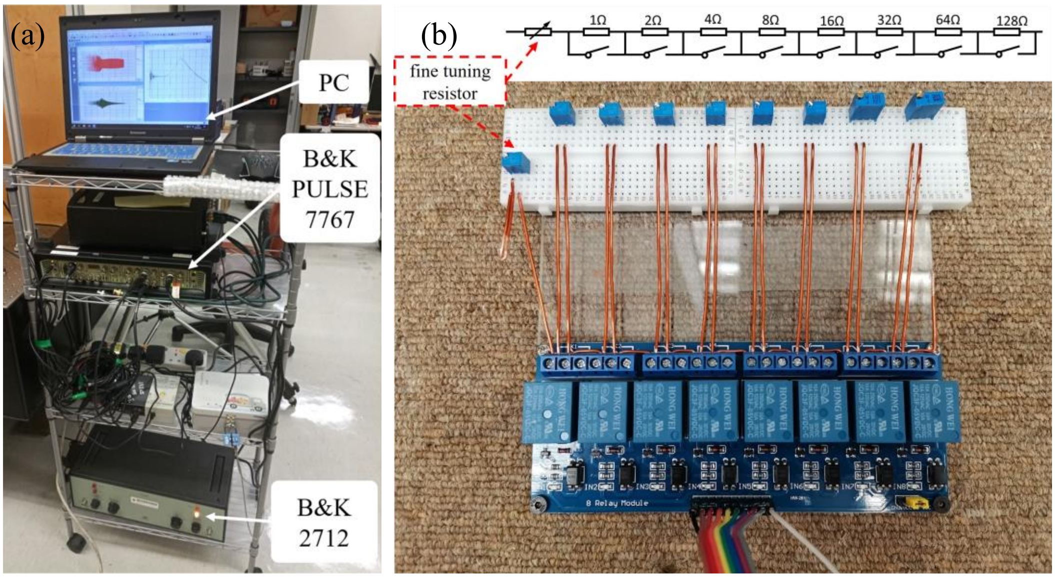

Fig. 16. Experiment auxiliary system: (a) the signal generation, data acquisition and processing system, (b) the tunable resistor

As shown in Fig. 16(a), a B&K PULSE 7767 is utilized for signal generation, data acquisition and processing. A B&K 2712 power amplifier is connected to the non-contact exciter to provide the input power of the primary system. The tunable resistor is combined with an 8-bit electromagnetic relay in Fig. 16(b) to change the external resistance in a binary system with 1 Ω resolution. A fine-tuning resistor is added to improve the resolution of the tunable resistor in case the resistance adjustment is smaller than 1 $\Omega$. The natural frequency of the primary system ($f_{n1} = 10.25\ \mathrm{Hz}$) can be obtained as shown in Fig. 17 through the free vibration response started with an initial displacement. The input energy demands identification for the energy flow qualification of the vibration system.

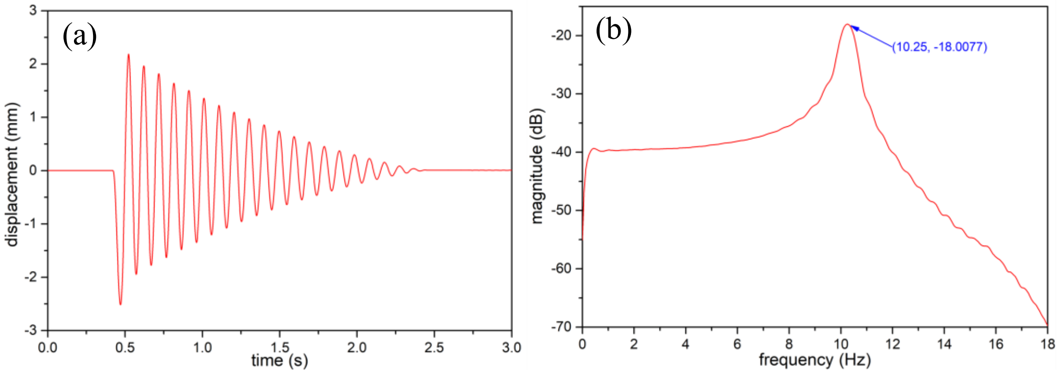

Fig. 17. Free vibration response of the primary system in (a) time domain, (b) frequency domain

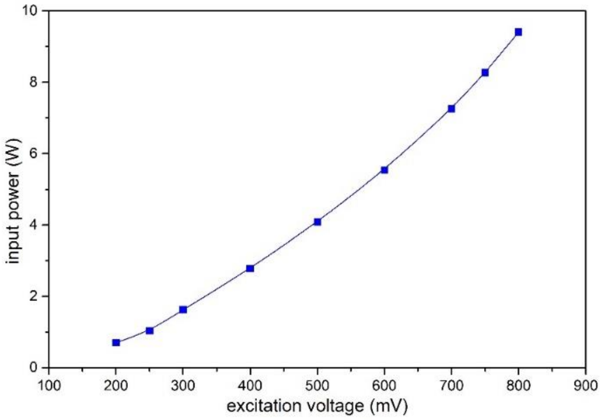

Fig. 18. Input energy power variation with different excitation voltage

In Fig. 18, the root-mean-square value of the vibrating system input energy with different excitation voltages is obtained by measuring the output voltage and the current of the B&K 2712 power amplifier.

### 4.2 SDOF system with EMSD

The vibration response and the harvested energy of the SDOF system with the proposed EMSD are measured in this section to verify the theoretical analysis results.

#### *4.2.1 Vibration response*

The displacement response of the SDOF system is shown in Fig. 19. As shown in Fig. 19(a), the maximum displacement always locates at the natural frequency regardless of the external resistance. A higher external resistance in the EMSD circuit corresponds to a lower damping and lower energy dissipation based on Eq.(2). Therefore, the maximum displacement response increases with the increase of the external resistance. Moreover, the maximum displacement amplitude variation with the external resistance matches with the theoretical prediction expressed by Eq. (9). The harvested energy is calculated by the measured voltage and the real-time external resistance of the tunable resistor in Fig. 19(b).

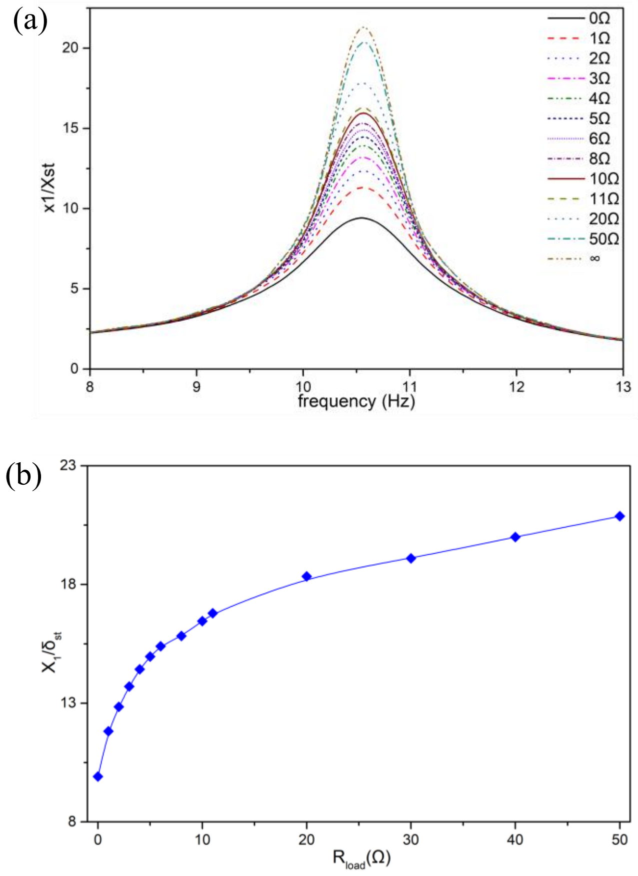

Fig. 19. SDOF system response: (a) the displacement amplitude variation in the frequency domain with different external resistance, (b) the normalized maximum displacement amplitude with different external resistance

### *4.2.2 Energy harvesting*

To locate the frequency for the maximum harvest energy, the harvested energy variation test in Fig. 20 with 0.25 Hz resolution indicates that the maximum harvested energy appears at 10.25 Hz which is the natural frequency of the primary system due to the maximum vibration velocity of the primary mass at resonance. Moreover, the harvested energy variation with external resistance at 10.25 Hz is much larger than that at other frequencies as shown in Fig. 21 because of the same reason.

As shown in Fig. 21, the harvested energy peaks with similar external resistance with excitation at five different frequencies. All the corresponding external resistances are larger than the internal impedance (2.5 Ω), particularly when the SDOF system is under the resonant excitation. One major reason for this phenomenon is that the internal impedance increases when the harvested energy increases dramatically.

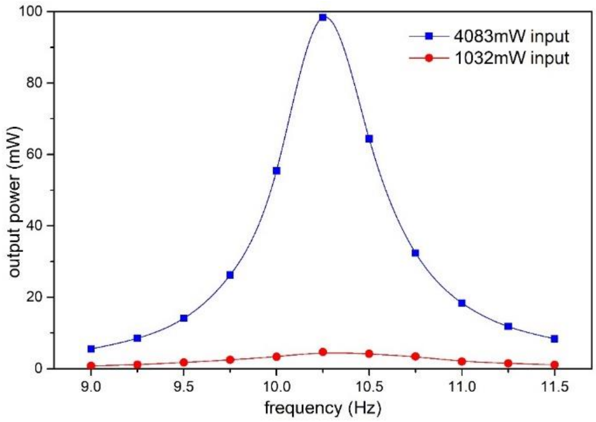

Fig. 20. Harvested energy variation of SDOF system in the frequency domain with 1Hz resolution

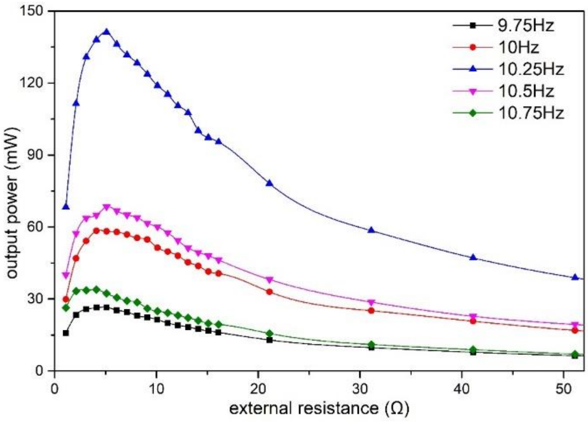

Fig. 21. Harvested energy variation of SDOF system with external resistance under different frequency excitation

### 4.3 DVA system with EMSD

The measured vibration response and the harvested energy of the DVA system with the proposed EMSD are presented in this section for the validation of the theoretical analysis results.

#### *4.3.1 Fixed-points calibration*

For the DVA system, fixed-points calibration is the top priority since the mini-maximum vibration response of the primary system occurs only with fixed-points of equal response magnitude in its response spectra. The response magnitude at the fixed-points can be tuned to equal by adjusting the DVA counter-weight as shown in Fig. 15.

Spectrum analysis of the primary system is conducted to observe the calibration effects. Three random values of external resistance are selected to find the intersections of the response curves under different damping. Once the two fixed points reach the same amplitude, the fixed points for optimal status are found. As shown in Fig. 22, properly calibrated fixed-points P and Q possess the same magnitude of the primary system response when the system is under the swept sinusoidal excitation from 0.1 Hz to 20 Hz with the speed of 1 Hz/s. Since the peak point of energy harvesting only depends on the resistance ratio while the vibration response depends on the resistance ratio and the transduction factor, the harvested energy is measured first with the searched identical fixed points.

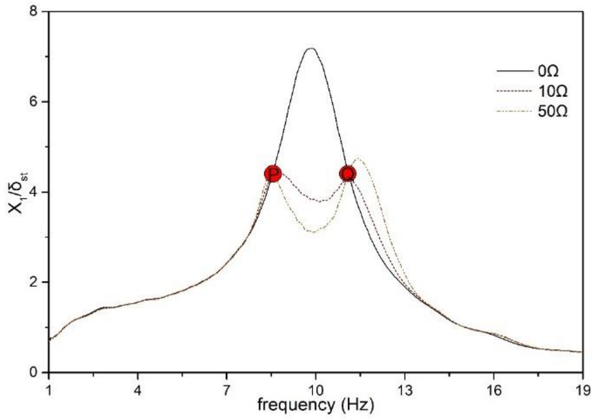

Fig. 22. Fixed-points calibration

### 4.3.2 Energy harvesting

Similar to the SDOF with EMSD system in Section B, the harvested energy test with 0.25 Hz resolution is shown in Fig. 23. The results show that the maximum harvested energy appears at frequency close to the fixed-point Q and varies with different energy input. As shown in Fig. 23, with 4083 mW energy input, the maximum harvested energy appears at frequency close to the fixed-point Q and the input energy does not cause much heat generation in the coils. The test case with 4083mW energy input is therefore selected for finding the relationship between the harvested energy and the effect of external resistance in the EMSD circuit for vibration control of the primary system.

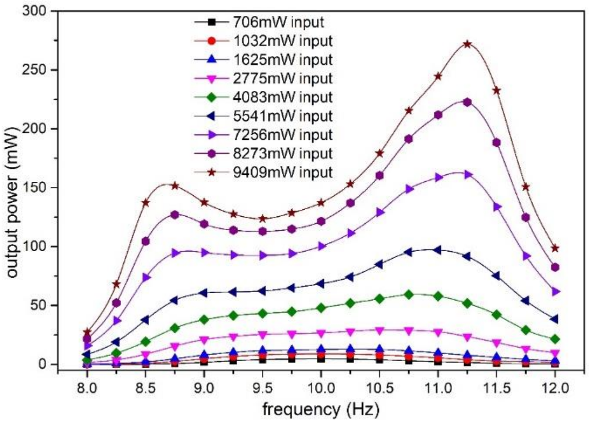

Fig. 23. Harvested energy variation of DVA system in the frequency domain with 1Hz resolution

As shown in Fig. 24, the harvested energy reaches the peak value with different external resistances in the EMSD circuit under different excitation frequencies. All the corresponding resistance values are larger than the internal impedance of 2.5 Ω. The major reason is that the internal impedance will increase when the harvested energy increase dramatically. The primary system response with different damping is identical and hence the same induced voltage (EMF) from the vibrating system at the fixed points of the response spectra of the primary mass. Moreover, the frequency of the fixed-point Q can be calculated as 10.79 Hz, which is close to 10.75 Hz. Therefore, the output power curve under 10.75 Hz excitation, whose peak value located at 6 Ω, is selected for the comparison of bi-objective optimal condition implementation.

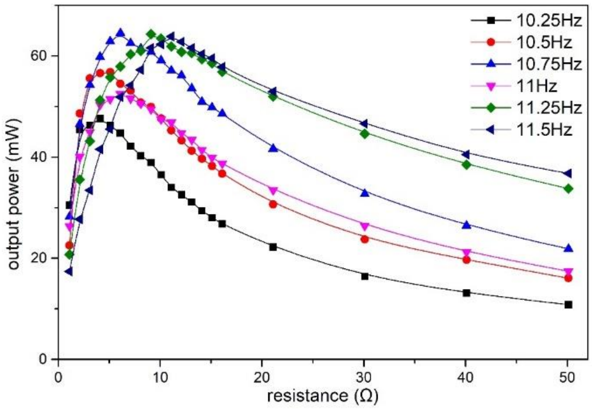

Fig. 24. Harvested energy variation of DVA system with external resistance under different frequency excitation

### 4.3.3 Vibration response

The primary system response measurement is conducted smoothly to reach the $H_\infty$ optimal status of the DVA system by tuning the external resistance with the properly tuned fixed-points as shown in Fig. 25. The optimal status appears when the external resistance is around 6 Ω at which the dimensionless response amplitudes of the primary system at the fixed points are equal and locate at the peaks of the response curve.

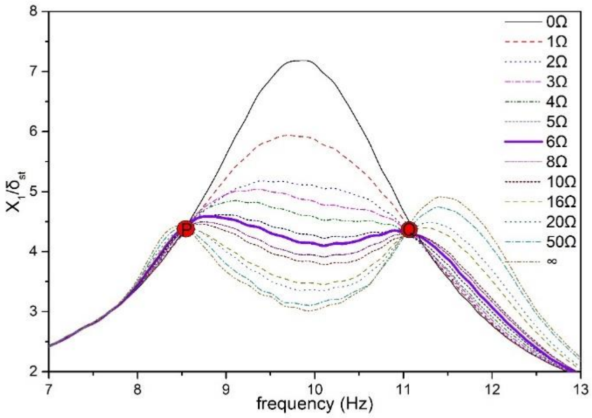

Fig. 25. Primary system response in the frequency domain with different external resistance when the proposed EMSD is applied in the DVA system, (a) the overall curve (b) zoom-in of the fixed-points

### 4.4 Bi-objective test results

The measured results of both vibration response and energy harvesting of the proposed EMSD when applied to a SDOF system (Fig. 15a) and to a DVA system (Fig. 15b) have been presented in the above sections. The harvested energy value is found to be much larger in the SDOF system than in the DVA system in comparison of the results in Fig. 26(a) and Fig. 26 (b). However, the proposed EMSD can harvest higher kinetic energy in a relatively broader frequency range in the DVA system than in the SDOF system.

The harvested energy and maximum amplitude of the primary system response at different external resistance in the EMSD circuit are plotted in Fig. 26. The harvested energy and the maximum vibration amplitude can obtain the optimal status with the same external resistance (around 6 Ω) in the DVA system, while the maximum vibration response increases monotonically in the SDOF system. Numerical results in terms of system response and harvested energy of the SDOF and DVA systems are added in Fig. 26(a) and Fig. 26(b), respectively, to compare with the measured results. It can be seen that the measured displacements and harvested energy match well with the predicted values, except the measured displacement in the DVA system, which is larger than the predicted one when the external resistance is higher than the optimal resistance. The possible reason behind is due to the diffrences in the damping ratio of the sensitive DVA system as a result of parasitic damping components in the system. Neverthless, the genral trend and even the energy level obtained numerrically and experimentally are deemed satisfactory to confirm the efficacy of the design.

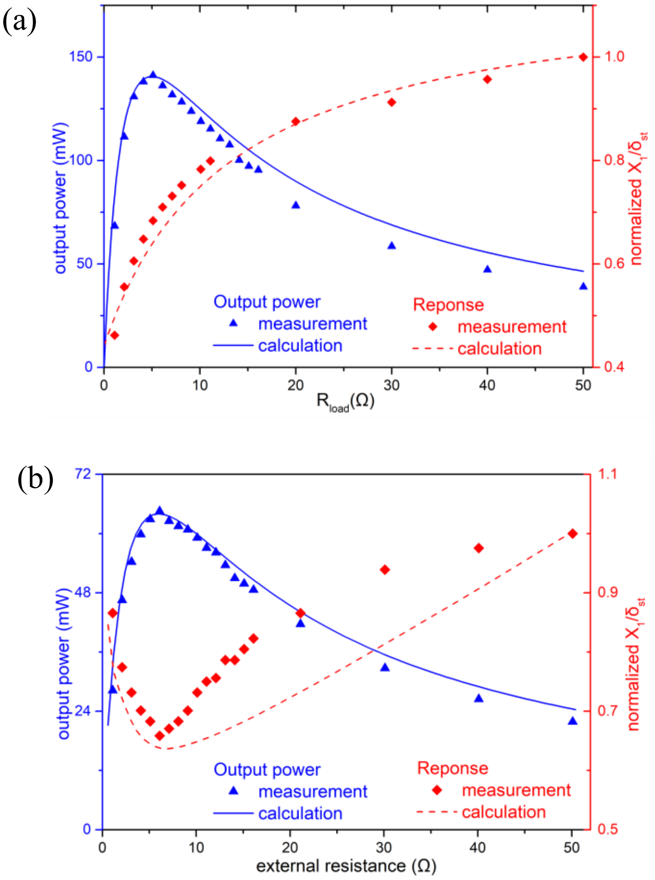

Fig. 26. Harvested energy and the maximum displacement response with different external resistance of (a) SDOF system, (b) DVA system

The steady-state response and energy harvesting performance are investigated with the proposed EMSD applied on a DVA system. For other applications where the excitation frequency changes considerably [29,30] and applications with intermittent [31] or time-limited [32] excitations, the applicability of the proposed EMSD is still required to be verified. The extending research of the proposed EMSD in these three aspects will be conducted in future.

## 5. Conclusions

A bi-objective optimal design methodology of EMSD is proposed and experimentally validated to achieve maximum amount of energy harvest from the damper and resonant vibration suppression of the vibrating structure simultaneously. To achieve maximum amount of energy harvest by the EMSD, its coil is designed such that its internal impedance equals to the external resistance in the EMSD circuit. By keeping the internal resistance of the EMSD coils constant, the transduction factor of the EMSD is adjusted to its optimum value leading to the optimum damping coefficient of the EMSD as dictated by the fixed-points theory of DVA. The electromechanical transduction factor is tuned by searching the optimal number of opposing magnet pairs numerically. It is found that EMSD with six opposing magnet pairs provides the optimal damping when the coil internal impedance equals external resistance. The proposed EMSD is applied to SDOF and DVA systems for both resonant vibration suppression and energy harvesting. The resonant vibration suppression increases monotonically with the decrease of resistance ratio in the SDOF system. On the other hand, the proposed EMSD provides maximum suppression of vibration amplitude of the primary mass and maximum energy harvested from itself as predicted by the theory. The bi-objective design methodology is applied and achieved in the DVA system as proven by the theoretical and experimental results. Moreover, the harvested energy is higher in the SDOF system than in the DVA, while the useful frequency bandwidth for energy harvesting is much wider in the DVA system.

## Acknowledgments

The authors would like to acknowledge the Research Grant Council of Hong Kong for the funding support (Project number: 15206120).

## References

[1] J. Ormondroyd, J.P. Den Hartog, The theory of the dynamic vibration absorber, Journal of Applied Mechanics, 50 (1928) 9–22.

[2] S. Behrens, A.J. Fleming, and S.O.R. Moheimani, Electromagnetic shunt damping, In Proc. AIM, IEEE, Kobe, Japan (2003) 1145-1150. https://doi.org/10.1109/AIM.2003.1225504

[3] R. Sun, W. Wong, and L.Cheng, Tunable electromagnetic shunt damper with opposing magnets configuration, Smart Materials and Structures, 29(11) (2020) 115034. https://doi.org/10.1088/1361-665X/abb21d

[4] B. Yan, H. Ma, W. Zheng, B. Jian, K. Wang, and C. Wu, Nonlinear electromagnetic shunt damping for nonlinear vibration isolators, IEEE/ASME Transactions on Mechatronics, 24.4 (2019) 1851-1860. https://doi.org/10.1109/TMECH.2019.2928583

[5] T. Ikegame, K. Takagi, and T. Inoue, Exact solutions to $H_\infty$ and $H_2$ optimizations of passive resonant shunt circuit for electromagnetic or piezoelectric shunt damper, Journal of Vibration and Acoustics, 141.3 (2019) 031015. https://doi.org/10.1115/1.4042819

[6] W. Ao and P. Reynolds, Evaluation of optimal analysis, design, and testing of electromagnetic shunt damper for vibration control of a civil structure, Structural Control and Health Monitoring, 27.3 (2020) e2495. https://doi.org/10.1002/stc.2495

[7] J. Li, S. Zhu, X. Shi, and W. Shen, Electromagnetic shunt damper for bridge cable vibration mitigation: full-scale experimental study, Journal of Structural Engineering, 146.1 (2020) 04019175. https://doi.org/10.1061/(ASCE)ST.1943-541X.0002477

[8] X. Xia, P. Liu, N. Zhang, D. Ning, M. Zheng, and H. Du, Takagi-Sugeno Fuzzy Control for the Semi-active Seat Suspension with an Electromagnetic Damper, In 3rd Conference on Vehicle Control and Intelligence, IEEE, Hefei, China (2019) 1-6. https://doi.org/10.1109/CVCI47823.2019.8951590

[9] A. Stabile, G. S. Aglietti, G. Richardson, and G. Smet, Design and verification of a negative resistance electromagnetic shunt damper for spacecraft micro-vibration, Journal of Sound and Vibration, 386 (2017) 38-49. https://doi.org/10.1016/j.jsv.2016.09.024

[10] R. Sun, W. Wong, and L. Cheng, Optimal design of a tunable electromagnetic shunt damper for dynamic vibration absorber, Mechatronics, 83 (2022) 102763. https://doi.org/10.1016/j.mechatronics.2022.102763

[11] Y. Shen, and K. Lu, Scavenging power from ultra-low frequency and large amplitude vibration source through a new non-resonant electromagnetic energy harvester. Energy Conversion and Management, 222 (2020) 113233. https://doi.org/10.1016/j.enconman.2020.113233

[12] M. Salauddin, H. Cho, and J.Y. Park, A Hybrid Electromagnetic-Triboelectric Energy Harvester Using a Dual Halbach Magnet Array Powered by Human-Body-Induced Motion, Advanced Materials Technologies, 3(2) (2018) 1700240. https://doi.org/10.1002/admt.201700240

[13] B. Lafarge, S. Grondel, C. Delebarre, O. Curea, and C. Richard, Linear electromagnetic energy harvester system embedded on a vehicle suspension: From modeling to performance analysis, Energy, 225 (2021) 119991. https://doi.org/10.1016/j.energy.2021.119991

[14] M.A.A. Abdelkareem, R. Zhang, X. Jing, X. Wang, and M.K.A. Ali, Characterization and implementation of a double-sided arm-toothed indirect-drive rotary electromagnetic energy-harvesting shock absorber in a full semi-trailer truck suspension platform, Energy, 239 (2022) 121976. https://doi.org/10.1016/j.energy.2021.121976

[15] Y. Pan, F. Liu, R. Jiang, Z. Tu, and L. Zuo, Modeling and onboard test of an electromagnetic energy harvester for railway cars, Applied Energy, 250 (2019) 568-581. https://doi.org/10.1016/j.apenergy.2019.04.182

[16] H. Liu, S. Gudla, F.A. Hassani, C.H. Heng, Y. Lian, and C. Lee, Investigation of the nonlinear electromagnetic energy harvesters from hand shaking, IEEE Sensors Journal, 15.4 (2014) 2356-2364. https://doi.org/10.1109/JSEN.2014.2375354

[17] K. Fan, M. Cai, H. Liu, and Y. Zhang, Capturing energy from ultra-low frequency vibrations and human motion through a monostable electromagnetic energy harvester, Energy, 169 (2019) 356-368. https://doi.org/10.1016/j.energy.2018.12.053

[18] Q. Cai and S. Zhu, Enhancing the performance of electromagnetic damper cum energy harvester using microcontroller: concept and experiment validation, Mechanical Systems and Signal Processing, 134 (2019) 106339. https://doi.org/10.1016/j.ymssp.2019.106339

[19] S. Zhu, W. Shen, and Y. Xu, Linear electromagnetic devices for vibration damping and energy harvesting: Modeling and testing, Engineering Structures, 34 (2012) 198-212. https://doi.org/10.1016/j.engstruct.2011.09.024

[20] M. Yuan, K. Liu, and A. Sadhu, Simultaneous vibration suppression and energy harvesting with a non-traditional vibration absorber, Journal of Intelligent Material Systems and Structures, 29.8 (2018): 1748-1763. https://doi.org/10.1177%2F1045389X17754263

[21] L. Zuo, and W. Cui, Dual-functional energy-harvesting and vibration control: electromagnetic resonant shunt series tuned mass dampers, Journal of Vibration and Acoustics, 135.5 (2013): 051018. https://doi.org/10.1115/1.4024095

[22] L. Xie, J. Li, X. Li, L. Huang, and S. Cai, Damping-tunable energy-harvesting vehicle damper with multiple controlled generators: design, modeling and experiment, Mechanical System and Signal Processing, 99 (2018): 859-872. https://doi.org/10.1016/j.ymssp.2017.07.005

[23] M. Zilletti, S.J. Elliott, and E. Rustighi, Optimisation of dynamic vibration absorbers to minimise kinetic energy and maximise internal power dissipation, Journal of Sound Vibration, 331.18 (2012): 4093-4100. https://doi.org/10.1016/j.jsv.2012.04.023

[24] Q. Cai, S. Zhu, and S. Ke, Can we unify vibration control and energy harvesting objectives in energy regenerative tuned mass dampers, Smart Materials and Structures, 29.8 (2020): 087002. https://doi.org/10.1088/1361-665X/ab92de

[25] W. Shen, S. Zhu, and H. Zhu, Experimental study on using electromagnetic devices on bridge stay cables for simultaneous energy harvesting and vibration damping, Smart Materials and Structures, 25.6 (2016): 065011. https://doi.org/10.1088/0964-1726/25/6/065011

[26] Y. Yin, B. Sun, and F. Han, Self-locking avoidance and stiffness compensation of a three-axis micromachined electrostatically suspended accelerometer. Sensors, 16(5) (2016) 711. https://doi.org/10.3390/s16050711

[27] G. Gatti, A.D. Shaw, P.J.P. Gonçalves, and M.J. Brennan, On the detailed design of a quasi-zero stiffness device to assist in the realisation of a translational Lanchester damper, Mechanical Systems and Signal Processing, 164 (2022) 108258. https://doi.org/10.1016/j.ymssp.2021.108258

[28] S.R. Khan, S.K. Pavuluri, and M.P.Y. Desmulliez, Accurate modeling of coil inductance for near-field wireless power transfer, IEEE Transactions on Microwave Theory and Techniques, 66.9 (2018):4158-4169. https://doi.org/10.1109/TMTT.2018.2854190

[29] S.H. Ju, H.T. Lin, and J.Y. Huang, Dominant frequencies of train-induced vibrations, Journal of Sound and Vibration, 319(1-2) (2009) 247-259. https://doi.org/10.1016/j.jsv.2008.05.029

[30] V.G. Cleante, M.J. Brennan, G. Gatti, and D.J. Thompson, Energy harvesting from the vibrations of a passing train: effect of speed variability. In Journal of Physics: Conference Series, 744(1) (2016) 012080. https://doi.org/10.1088/1742-6596/744/1/012080

[31] G. Yang, B.H. Stark, S.J. Hollis, and S.G. Burrow, Challenges for energy harvesting systems under intermittent excitation, IEEE Journal on Emerging and Selected Topics in Circuits and Systems, 4(3) (2014). 364-374. https://doi.org/10.1109/JETCAS.2014.2337172

[32] M.J. Brennan, and G. Gatti, Harvesting energy from time-limited harmonic vibrations: mechanical considerations, Journal of Vibration and Acoustics, 139(5) (2017) 051019. https://doi.org/10.1115/1.4036867